

Influence of Extreme Flow Channeling on the Thermal Performance of Open-Loop Geothermal Systems at Commercial Scale

Patrick M. Fulton (✉ pfulton@cornell.edu)

Department of Earth and Atmospheric Sciences <https://orcid.org/0000-0002-6259-2369>

Nicolas Rangel Jurado

ETH Zürich D-ERDW: Eidgenössische Technische Hochschule Zurich Departement Erdwissenschaften
<https://orcid.org/0000-0001-7384-4448>

Adam J. Hawkins

Smith School of Chemical and Biomolecular Engineering

Research

Keywords: Thermal performance, fluid flow short-circuiting, enhanced geothermal systems, reservoir management strategies

Posted Date: March 21st, 2022

DOI: <https://doi.org/10.21203/rs.3.rs-1454926/v1>

License:  This work is licensed under a Creative Commons Attribution 4.0 International License.
[Read Full License](#)

1 **Influence of Extreme Flow Channeling on the Thermal Performance**
2 **of Open-Loop Geothermal Systems at Commercial Scale**

3 Nicolás Rangel-Jurado^{1,2}, Adam J. Hawkins¹, Patrick M. Fulton¹

4 ¹Cornell University, Ithaca, NY, USA

5 ²Now at ETH Zurich, Zurich, Switzerland

6
7 Corresponding author: pfulton@cornell.edu

8 **Abstract**

9 Adequate stewardship of geothermal resources requires accurate forecasting of long-term thermal
10 performance. In enhanced geothermal systems and other fracture-dominated reservoirs, predictive
11 models commonly assume constant-aperture fractures, although spatial variations in aperture can
12 greatly affect reservoir permeability, fluid flow distribution, and heat transport. Whereas previous
13 authors have investigated the effects of theoretical random aperture distributions on thermal
14 performance, here we further explore the influence of permeability heterogeneity considering
15 field-constrained aperture distributions from a meso-scale field site in northern New York, USA.
16 Using numerical models of coupled fluid flow and heat transport, we conduct thermal-hydraulic
17 simulations for a hypothetical reservoir consisting of a relatively impervious porous matrix and a
18 single, horizontal fracture. Our results indicate that in highly channelized fields, most well design
19 configurations and operating conditions result in extreme rates of thermal drawdown (e.g., 50%
20 drop in production well temperatures in under two years). However, some other scenarios that
21 account for the risks of short-circuiting can potentially enhance heat extraction when mass flow
22 rate is not excessively high, and the direction of geothermal extraction is not aligned with the most
23 permeable features in the reservoir. Through a parametric approach, we illustrate that well
24 separation distance and relative positioning play a major role in the long-term performance of
25 highly channelized fields, and both can be used to help mitigate premature thermal breakthrough.

26 **Keywords:** Thermal performance, fluid flow short-circuiting, enhanced geothermal systems,
27 reservoir management strategies.

28 **Introduction**

29 Geothermal energy has the potential to provide carbon-free, baseload and renewable energy for
30 several generations to come. However, uncertainty in forecasting the commercial lifetime of a site-
31 specific geothermal system remains a considerable barrier to attracting investment capital (e.g.,
32 Watanabe et al., 2010; Pandey & Vishal, 2017). Among other technical challenges for geothermal
33 energy, thermal interference between cold injectors and hot producers, or “short-circuiting”, can
34 result in substantial drops in production temperature that endangers the reservoirs’ long-term
35 commercial success (Tsang & Neretnieks, 1997; Kolditz & Clauser, 1998; Hui et al., 2018). This
36 concern is particularly true in Enhanced Geothermal Systems (EGS) as fluid flow is expected to
37 concentrate in fractures and other narrow flow channels that reduce the effective inter-well surface
38 area available for heat transfer (Murphy et al., 1981; Brown, 1987; Lu, 2018). Existing literature
39 addressing this issue has determined the range of uncertainties for a single discrete rock fracture
40 with non-uniform fracture aperture (e.g., Fox et al., 2015; Ghassemi et al., 2015). However, the
41 statistical descriptions of the aperture variability largely reflect small-scale (cm) measurements on
42 rock core, which in most cases fail to represent a reasonable representative elementary volume for
43 large-scale reservoirs (Corbett et al., 1998; Farmer, 2002).

44 Alternatively, Neuville et al (2010) and Fox et al. (2015) discuss the influence of fluid flow short
45 circuits on the thermal behavior of single-fracture geothermal reservoirs using randomly
46 generated, self-affine aperture fields. However, a recent meso-scale field demonstration presented
47 in Hawkins et al (2020) suggests that field-scale “realistic” fractures may suffer from flow
48 channeling more acutely than suggested by previous studies that adopted core-scale aperture
49 statistics at the reservoir-scale. This, in addition to other issues like limited availability and sparsity
50 of permeability data at reservoir scale, often make going from theoretical studies to site-specific
51 predictive models a challenging endeavor (Smith, 2019). Here, we utilize a rare and interesting
52 data set of fracture aperture variations characterized at a meso-scale (~14 m) field site and use their

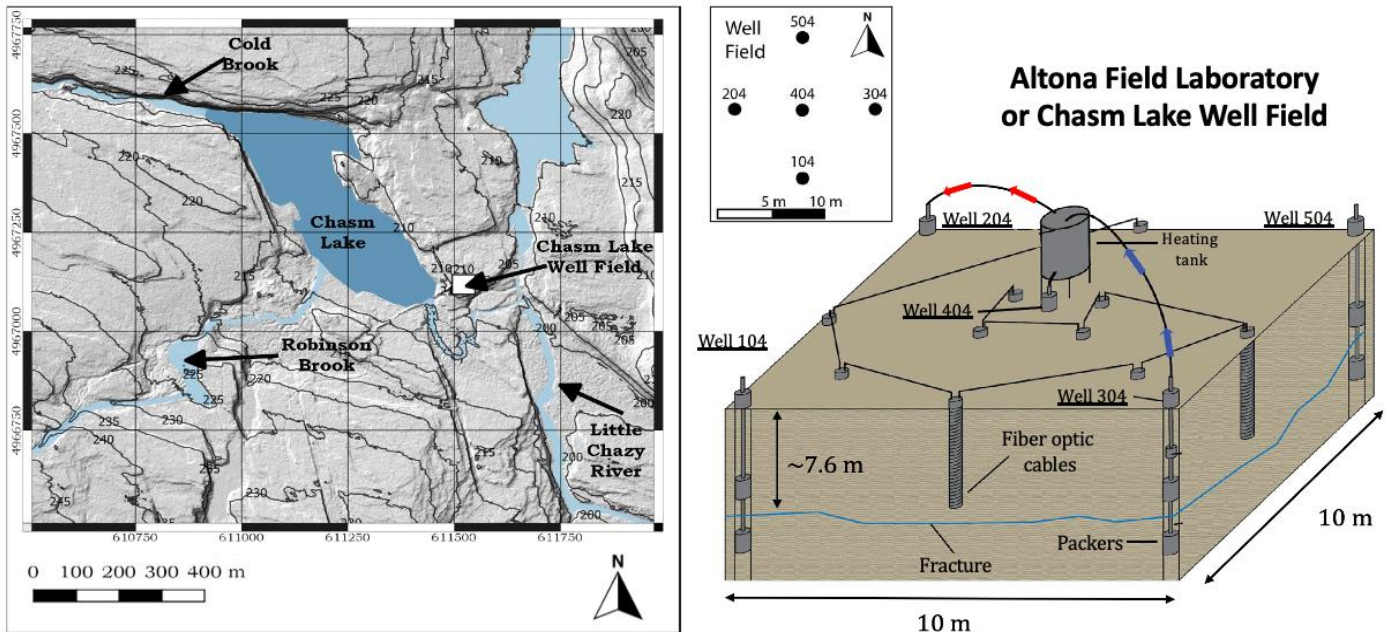
53 statistical distribution to extrapolate and assess their impact on the commercial-scale (100's of
54 meters).

55 In this work, we test the effects of the extreme short-circuiting effects identified at meso-scale by
56 Hawkins et al. (2020) at the commercial-scale, where project lifetimes of 10 to 30 years are desired.
57 For this, we simulate heat extraction in a single fracture within a large-scale geothermal reservoir
58 and utilize a fully coupled thermal-hydraulic model with an empirically-derived, up-scaled
59 permeability distribution. Using the best-fit aperture distribution from Hawkins et al. (2020), 13
60 different well-pair configurations are considered to determine the thermal performance variability
61 at commercial scale using field-measured trends in the spatial distribution of fracture aperture. In
62 our simulations, we consider variations in: (1) separation distance between wells; (2) mass flow
63 rates; and (3) relative well locations within the non-uniform fracture aperture plane. The objective
64 of this study is to assess the implications of short-circuiting at the commercial scale, including: 1)
65 reservoir sizing and optimization of mass flow rates, 2) optimal locations for injection and
66 production wells, and 3) potential reservoir management strategies to mitigate resource
67 deterioration.

68 In order to study the thermal-hydraulic behavior of inlet-outlet short-circuiting in a single-fracture
69 circumstance, we use a field-validated fracture aperture distribution identified via machine
70 learning (genetic algorithm) based on the combined results of tracer testing, geophysical imaging,
71 and hydraulic measurements. These data were collected between 2014 and 2017 at the Altona Field
72 Laboratory (i.e., "Altona"), which is located ~6 km northwest of West Chazy, New York in
73 northeastern New York state near the borders with Canada and Vermont (Figure 1). Altona has
74 been extensively used for studying fracture-dominated fluid flow, heat transfer, and chemical
75 transport processes (Hawkins et al., 2017a, 2017b, 2018, 2020, 2021). The geologic formation of
76 interest, the Cambrian-aged Potsdam Sandstone, is a well-cemented stratigraphic unit with low
77 primary (i.e., matrix) porosity (~1%) but widespread and naturally-occurring secondary porosity

78 (i.e., fractures) which makes the crystalline rock formation highly permeable (Rayburn et al., 2005;
79 Olcott, 1995).

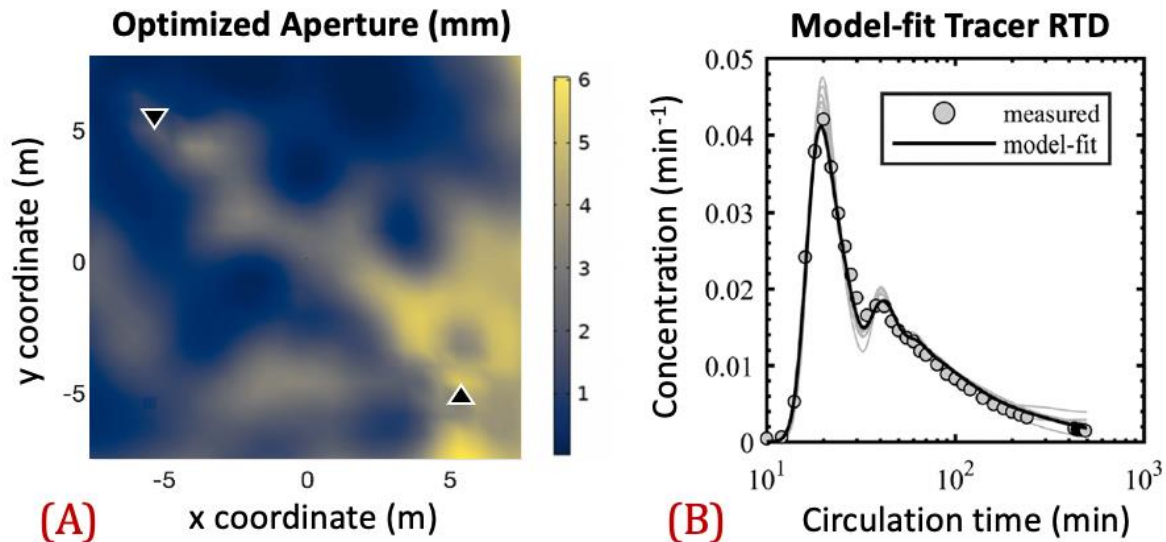
80 A five-spot well configuration has been drilled at Altona within a 10 x 10 m square. Of interest to
81 this study, all five wells intersect a highly conductive fracture oriented sub-horizontally at a depth
82 of roughly 7.6 m below ground surface. The ambient temperature within the fracture is $\sim 12^\circ\text{C}$.



84 **Figure 1.** On the left, a Digital Elevation Map (DEM) of the region surrounding the Altona Field Laboratory
85 in upstate New York, USA. White rectangle represents the approximate location of the five-spot well field
86 (Taken and modified from Hawkins, 2017). On the right-hand side, a three-dimensional schematic of Altona
87 showing the 5-well configuration. Red and blue arrows depict the circulation of fluids being injected into
88 the reservoir at high temperatures and being pumped back up to the surface to be heated through a tankless
89 water heater and re-injected again, forming a fluid circulation loop (Taken and modified from Hawkins,
90 2017).

91 In 2015 and 2016, experiments using a variety of tracers: some inert, some adsorptive, and some
92 thermally-degrading were conducted at this site to characterize the fracture-dominated reservoir
93 flow paths (Hawkins et al, 2018). Using the breakthrough curve of one of the inert tracers (inert c-
94 dot nanoparticles) and the frictional pressure loss between well 204 and well 304, Hawkins et al.
95 (2020) derived a spatial distribution for the 2D permeability field at Altona via machine learning
96 (a genetic algorithm) and Principal Component Analysis (PCA). This optimized aperture

97 distribution is presented in Figure 2 panel A. In addition, Figure 2 panel B shows the measured
98 and simulated tracer breakthrough curves for the inert tracer test experiment during roughly 500
99 min of fluid circulation alongside the model fit conducted using the best-fit aperture distribution
100 in Panel A.



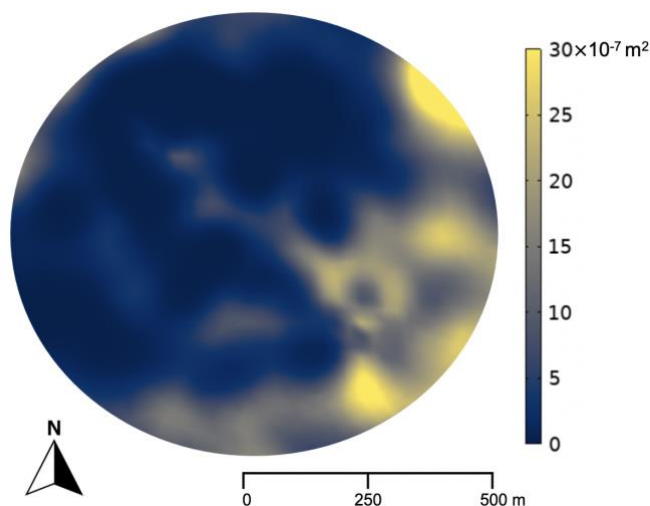
101
102 **Figure 2.** Panel A: Best fit aperture distribution calibrated by frictional pressure loss and an inert tracer test. Black
103 triangles represent the location of the injection and production wells. Panel B: Measured and simulated RTDs for inert
104 tracers throughout 6 days of fluid circulation. Note that lighter gray lines represent multiple repetitions of the machine
105 learning algorithm, while the black line represents the repetition that provided the best agreement with field observations.
106 Highlighted model fit in Panel B used the best fit aperture distribution in Panel A as input. (Adapted from Hawkins et al.,
107 2020).

108 **Methods**

109 To calculate how *realistic* fracture aperture distributions can affect heat transfer processes in
110 geothermal reservoirs, we employ a numerical model that simulates the thermal-hydraulic
111 behavior of a single-fracture reservoir displaying Altona’s up-scaled aperture distribution. For this,
112 we use COMSOL Multiphysics 5.6., which is a finite element method (FEM) numerical software
113 that solves partial differential equations (PDEs) of coupled multi-physical phenomena and is
114 employed broadly in a variety of scientific and engineering settings (COMSOL 2019). For
115 instance, our 3D conductive-advective reservoir model fully couples the heat transfer from the
116 bulk rock assuming 3D thermal conduction in the rock matrix while simultaneously solving the

117 governing equations of fluid flow and heat transfer in the 2D fracture based on the tangential
118 derivatives along the internal boundary representing the fracture.

119 By considering field-constrained aperture distributions—derived from empirically-collected
120 data—we evaluate the impact of operational design considerations on thermal performance. To do
121 this we up-scale the permeability distribution at Altona using a simple renormalization technique
122 by multiplying the spatial coordinates of optimized aperture distribution in Figure 2 Panel A by a
123 scale factor of 42.55 such that a previous well separation of 14.1 m at Altona, corresponds to a
124 well separation length of 600 m in the upscaled model (Figure 3). The resulting permeability
125 distribution covers a circular area with radius of 500 m and the orientation of the fracture is such
126 that due North is aligned with the positive y-axis.



127
128 **Figure 3.** Upscaled permeability distribution from Altona for a synthetic circular region of 500 m of radius. The
129 permeability distribution was rescaled using a renormalization technique for the x and y coordinates ($dx \rightarrow k \cdot dx$,
130 $dy \rightarrow k \cdot dy$) where k is 42.55. Permeability is expressed in m^2 units. Orientation of the fracture was shifted so due
131 North is aligned with the positive y-axis.

132 By upscaling the geometry and statistical appearance of the original rock surface, we are able to
133 assess extraction parameters appropriate for utility-scale geothermal fields, while preserving the
134 original spatial correlation of self-affine rock surfaces (Yavari et al., 2002). Our *local-global* up-
135 scaling technique is not intended to be representative of the regional permeability surrounding the
136 Altona Field Laboratory. Instead, it represents a synthetic, self-affine permeability distribution for

137 a large-scale reservoir displaying a highly channelized hydrogeological behavior. This approach
138 resembles similar methodologies employed by Candela et al. (2009), Glover et al (1998), and
139 Gómez-Hernández & Journel (1990).

140 With the resulting permeability distribution, we conduct a sensibility analysis for three attributes
141 that reflect design/operating parameters in a commercial scale setting. These attributes are: (1)
142 mass flow rate (10 to 40 kg·s⁻¹); (2) well separation distance (300 to 500 m); and (3) four different
143 flow orientations relative to North. The range of parameter values considered is listed in Table 2.
144 Temperature-dependent thermodynamic properties of the fluid are modeled, and no-flow
145 boundaries are specified surrounding the outer dimensions of the model domain. The range of
146 operational and pressure conditions modeled in this study ensure that water remains in the liquid
147 state, thus, the effects of flashing are not considered.

148 Laminar fluid flow in a single fracture can be described analytically by the Hele-Shaw equation,
149 also known as the “cubic law” (Witherspoon et al., 1980; Zimmerman & Bodvarsson, 1994):

$$150 \quad Q = \frac{b^3 w \Delta P}{12 \mu L} \quad s. t. \quad w \gg b. \quad (1)$$

151 where Q is the volumetric flow rate, b is the fracture aperture, w is the fracture width, ΔP is the
152 frictional pressure loss, μ is the dynamic viscosity of the fluid, and L is the length of the fracture
153 channel. The use of this analytical solution assumes the fluid to be viscous and incompressible.
154 Comparing Equation 1 with Darcy’s Law, where specific discharge (q) equals permeability of the
155 medium (k) times the pressure drop (Δp) divided by the product of the characteristic distance (L)
156 and the dynamic viscosity of the fluid (μ), it is possible to express the permeability of a fracture
157 (k_f) in terms of its fracture aperture (b) as:

$$158 \quad k_f = \frac{b^2}{12} \quad (2)$$

159 Thus, a fracture bounded by two smooth, parallel plates separated by a constant aperture will
160 exhibit a homogenous permeability. In contrast, for non-uniform fractures, permeability is
161 spatially variable. Equation 2 shows how fracture aperture can be treated as an analog for

162 permeability in fractured media; thus, these two terms are used interchangeably throughout this
163 work when appropriate.

164 For naturally-fractured reservoirs or enhanced geothermal systems (EGS), fluid flow and heat
165 transport will preferentially occur along rock fractures since these are usually orders of magnitude
166 more permeable than the host matrix (National Research Council, 1996). As circulating fluids
167 between injectors and producers will be largely concentrated within the individual fractures, the
168 conservation of mass for a Newtonian fluid in a single-fracture reservoir can be written as:

$$169 \quad b \frac{\partial}{\partial t} (\rho_w) + \nabla_T (b \rho_w u_f) = b Q_m \quad (3)$$

170 where t is transient time, ρ_w the water or working fluid density, ∇_T indicates the gradient operator
171 restricted to the fracture's tangential plane, u_f is the Darcy velocity of the fluid inside the fracture,
172 and Q_m is the mass source term. Note that the velocity field can be spatially variable in accordance
173 with the aperture field and locations of sinks/sources, but it remains constant over time at all points
174 as long as the pressure conditions along the fracture are not altered. This velocity field term can
175 also be expressed as:

$$176 \quad u_f = -\frac{k_f}{\mu} (\nabla_T p + \rho g) \quad (4)$$

177 where p is the pressure and g is the local acceleration due to gravity. Equation 3 relates the mass
178 transfer to the fracture from media source/sink (e.g., injection/production well) where fracture
179 aperture b can vary spatially within the two-dimensional fracture plane. Equation 3 is then solved
180 to calculate the pressure field and the corresponding velocity field is calculated with Equation 4.
181 The fracture is confined by no-flow boundaries in the x-direction meaning no mass flow is allowed
182 through the spatial boundaries of the model domain. Hence, the reservoir is assumed to be
183 hydraulically isolated from the surrounding formation.

184 The heat transfer in this system occurs both in the bulk rock matrix through conduction and in the
 185 fracture via forced advection. Thermal conduction in the bulk rock matrix is governed by the three-
 186 dimensional thermal diffusion equation:

$$187 \quad (\rho C_p)_{eff} \frac{\partial T}{\partial t} = -\rho_w C_{p.w} u \cdot \nabla T - \nabla \cdot (-k_{eff} \nabla T) + Q_{th} \quad (5)$$

$$188 \quad (\rho C_p)_{eff} = (1 - \phi_r) \rho_r C_{p.r} + \phi_r \rho_w C_{p.w} \quad (6)$$

189 where $(\rho C_p)_{eff}$ is the effective volumetric heat capacity for the bulk rock matrix, T is the
 190 temperature of the rock, ϕ_r is the rock porosity, k_{eff} the effective thermal conductivity of the bulk
 191 rock matrix, ρ_r and $C_{p.r}$ are the density and specific heat capacity of the rock, respectively, and
 192 Q_{th} is the heat flux term that corresponds to a position on the two-dimensional fracture plane. The
 193 heat transfer equilibrium between the bulk rock matrix and the fracture is derived from the
 194 conservation of energy law and is given by the following equation:

$$195 \quad b(\rho C_p)_{eff.f} \frac{\partial T}{\partial t} = -b \rho_w C_{p.w} u_f \cdot \nabla_T T - \nabla_T \cdot (-b k_{eff.f} \nabla_T T) + b Q_{th.f} \quad (7)$$

196 where the subscript f corresponds the properties within the fracture. The heat source term in the
 197 fracture $Q_{th.f}$ is related to the rate of advection along the fracture surface and it is coupled to the
 198 thermal conduction from the bulk rock matrix in Equation 6. As a result, Equations 5 and 7 are
 199 solved simultaneously to determine the surface heat flux between the fracture and the bulk rock
 200 matrix. Thermal energy transfer between the rock and the fluid is assumed to be at local
 201 equilibrium, which means that the temperature of the fluid within the fracture aperture is in
 202 equilibrium with the fracture-matrix interface. This relationship is given by the following
 203 equations:

$$204 \quad T(x, y, z, t) = T \quad (8)$$

205 where T is the temperature of both the rock and the fluid at all times t in a given point $p(x, y, z)$.

206 The governing equations are restricted to initial and boundary conditions as follows:

$$207 \quad T(x, y, z, 0) = T_{res} \quad (9)$$

208
$$T(x_i, y_i, z_i, t) = T_{inj}, \quad t > 0 \quad (10)$$

209 Equation 9 implies that at time equal to zero, the rock and fracture fluids will be at a constant
 210 reservoir temperature T_r , whereas Equation 10 indicates that the injection point will remain at a
 211 constant reinjection temperature T_{inj} for all times greater than zero where the fluid is being injected
 212 at a constant mass flow rate \dot{m} . As a result, the temperature at the production well and the thermal
 213 output for the system are the key variables of interest and are dependent on time:

214
$$T_{prod}(t) = T(x_{prod}, y_{prod}, z_{prod}, t) \quad (11)$$

215
$$\dot{Q}(t) = \dot{m}C_{p,f}(T_{prod} - T_{inj}) \quad (12)$$

216 Where heat rate or heat production \dot{Q} depends on time and is measured in watts. As a final step, it
 217 is beneficial for results analysis to normalize this production temperature to a dimensionless value
 218 that is bounded between zero and 1, as indicated by the following equation:

219
$$T_{nd} = \frac{(T_{prod} - T_{inj})}{(T_r - T_{inj})} \quad (13)$$

220 Therefore, when the production temperature of the fluid equals that of the reinjection temperature,
 221 the dimensionless temperature T_{nd} is equal to zero, indicating absolute thermal depletion of the
 222 reservoir. Meanwhile, a value of unity for T_{nd} means that the production fluid is at the same
 223 temperature as the original reservoir temperature before the geothermal operation began.

224 Fluid density and dynamic viscosity vary as a function of temperature and pressure. However,
 225 under the typical conditions of low-enthalpy geothermal reservoirs, the fluid properties of water
 226 are mainly dependent on temperature (Bundschuh & Suárez-Arriaga, 2010). Another common
 227 simplification in subsurface reservoir modeling is that fluid viscosity and density can be considered
 228 as constant for low-enthalpy geothermal systems. However, for most fluids, as temperature rises,
 229 liquids commonly become less dense and less viscous. Our simulations consider the effect of
 230 temperature-dependent variations in viscosity (ranging from 0.0018 to 0.002 Pa·s) and density

231 (ranging from $1000 \text{ kg}\cdot\text{m}^{-3}$) based on the empirical approximations reported by Chandrasekharam
 232 and Bundschuh (2008) for temperatures between 0 and $150 \text{ }^\circ\text{C}$:

233

$$234 \quad \rho(T) = \begin{cases} 1000.0 \cdot (1.0 - 8.0 \cdot 10^{-6} \cdot (T - 3.98)^2), & 0^\circ\text{C} \leq T \leq 20^\circ\text{C} \\ 996.9 \cdot (1.0 - 3.17 \cdot 10^{-4}(T - 25.0) - 2.56 \cdot 10^{-6} \cdot (T - 25.0)^2), & 20^\circ\text{C} \leq T \leq 150^\circ\text{C} \end{cases} \quad (14)$$

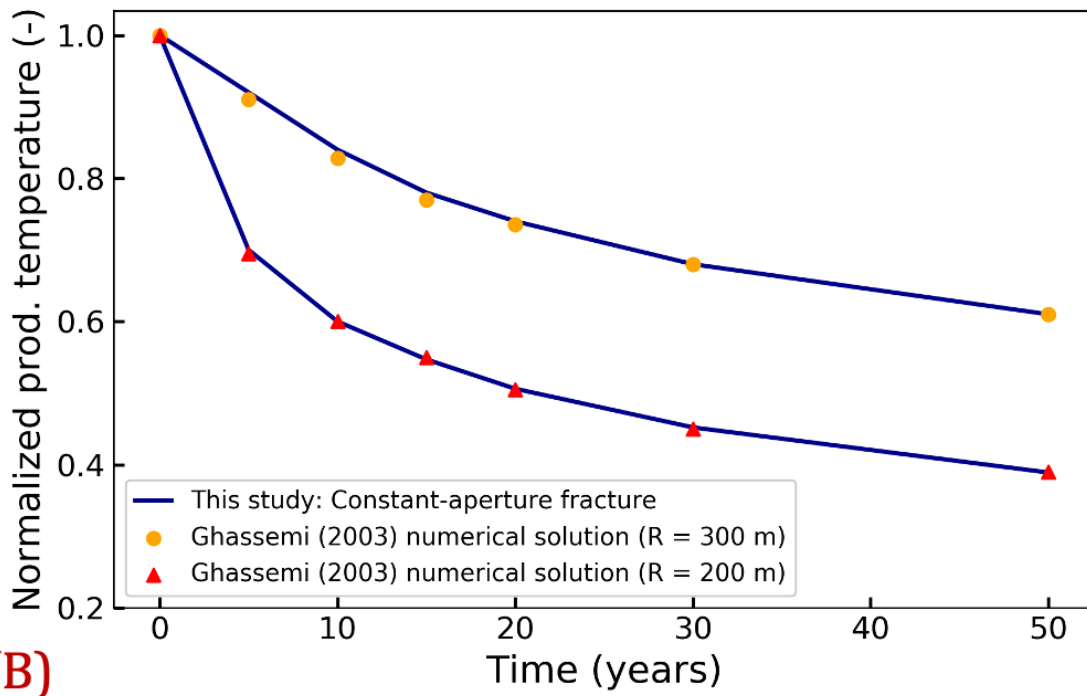
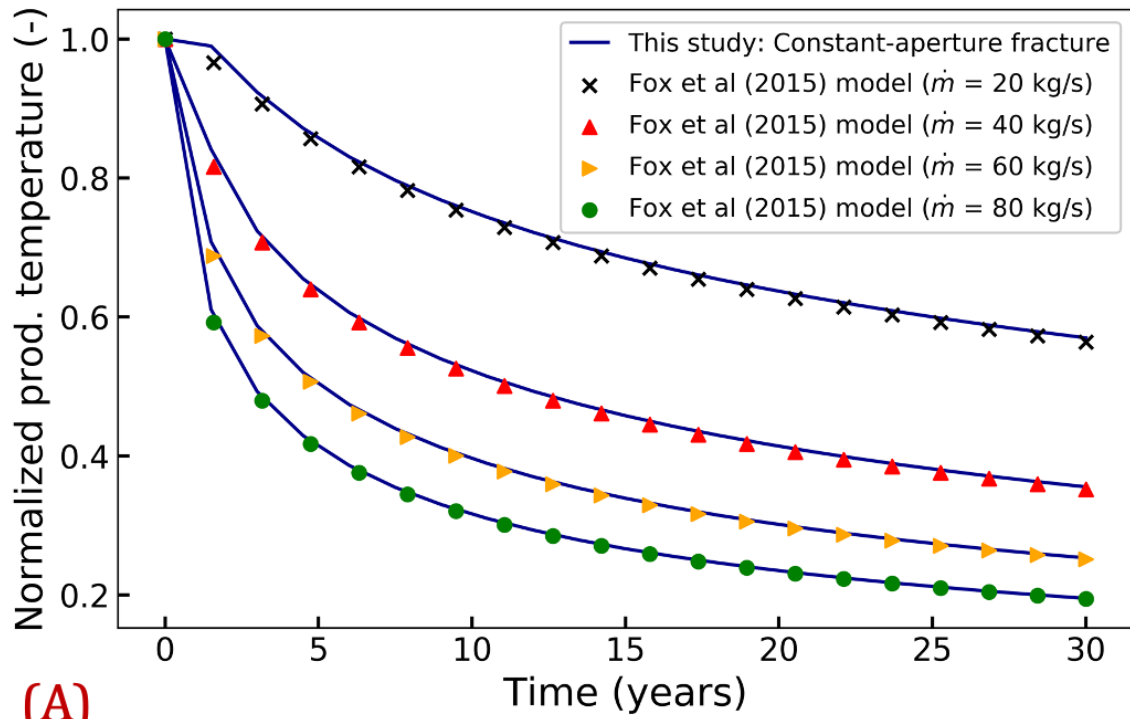
$$235 \quad \mu(T) = \begin{cases} 10^{-3} \cdot (1.0 + 0.015512(T - 20.0))^{-1.572}, & 0^\circ\text{C} \leq T \leq 100^\circ\text{C} \\ 241.4 \cdot 10^{-7} \cdot 10^{\frac{247.8}{T+133.15}}, & 100^\circ\text{C} \leq T \leq 150^\circ\text{C} \end{cases} \quad (15)$$

236 To ensure that our numerical model is accurate, we validate our results with benchmark solutions
 237 for fluid flow and heat transfer in uniform-aperture fractures (e.g. Fox et al., 2015; Ghassemi et
 238 al., 2003). Both Fox et al. and Ghassemi et al. use an alternative approach to the one implemented
 239 in our models. They solved for the heat transfer in the porous medium analytically and solved the
 240 fracture flow equations numerically (see references for details). In contrast, we model both fluid
 241 flow in the fracture and in the bulk rock matrix numerically. The bulk rock matrix that surrounds
 242 the permeable fracture is discretized in 3D while fluid flow within the fracture is reduced to a 2D
 243 system based on the tangential derivatives along the internal boundary to optimize the computation
 244 efficiency (Bruderer-Weng et al. 2004).

245 As shown in Figure 4, both hybrid numerical-analytical models by Fox et al. and Ghassemi et al.
 246 are in good agreement with our purely numerical COMSOL model. Figure 4 panel A depicts the
 247 results comparison between our model and that of Fox et al. for different values of mass flow rate
 248 through a circular fracture with a radius of 500 m displaying uniform aperture distribution and an
 249 inter-well separation distance of 600 m. Similarly, Figure 4 panel B shows the comparison with
 250 the model of Ghassemi et al. for which mass flow rate was fixed at 80 kg/s but two different
 251 fracture sizes and inter-well separation distances were evaluated. The first simulation considers a
 252 fracture size R of 200 m while the fracture size in the second simulation is increased to 300 m;
 253 injection and extraction wells are located at $\pm R/2$ on the x-axis in both cases. These parameters
 254 and the remaining modeling parameters for both simulations are specified in Table 1.

255 Table 1. Summary of the modeling parameters for the cross-validation with benchmark solutions. Values
 256 specified in the third and fourth columns correspond to values reported by Fox et al. (2015) and Ghassemi
 257 et al. (2003), respectively.

Parameter	Symbol	Values for Fox et al. (2015) validation	Values for Ghassemi et al. (2003) validation
Uniform fracture aperture	b	5 mm	5 mm
Specific heat capacity of the fluid	$C_{p,f}$	4184 J/(kg·K)	4050 J/(kg·K)
Specific heat capacity of the rock	$C_{p,r}$	1000 J/(kg·K)	1100 J/(kg·K)
Thermal conductivity of the fluid	k_f	0.6 W/(m·K)	0.6 W/(m·K)
Thermal conductivity of the rock	k_r	2.40 W/(m·K)	2.58 W/(m·K)
Dynamic viscosity of the fluid	μ	1E-3 Pa·s	1E-3 Pa·s
Fluid density	ρ_f	1000 kg/m ³	1000 kg/m ³
Rock density	ρ_r	2300 kg/m ³	2650 kg/m ³
Reinjection temperature	T_{inj}	50°C	60°C
Reservoir temperature	T_r	200°C	140°C



258

259

260

261

Figure 4. Model validation results with benchmark solutions for single-fracture reservoirs displaying uniform aperture. Panel A) Model comparison with Fox et al (2015). The graph shows simulations for four different mass flow rates (20, 40, 60, and 80 kg/s). Panel B) Model comparison with Ghassemi et al (2003). Graph shows

262 simulations for two fracture lengths (200 and 300 m). The rest of modeling parameters for both validations are
 263 contained in Table 1.

264 After validating the accuracy of our model, we proceed to conduct sensitivity analyses where we
 265 assess the influence of three attributes on the commercial-scale thermal performance of the
 266 reservoir. In particular we vary: mass flow rate (10 to 40 $kg \cdot s^{-1}$), well separation distance (300
 267 to 500 m), and well relative placement along four different orientations. The experimental chart in
 268 Table 2 shows the specific way in which the parameters are modified for nine different simulations.
 269 Here, the influences of the three attributes of interest outlined above are individually added and
 270 assessed for each set of cases while keeping all other parameters fixed. Table 3 shows the
 271 parameters that remain constant for all nine simulations.

272

273 **Table 2.** List of cases simulated. Case 0 represents the base case of an ideal fracture displaying constant
 274 aperture. The subsequent cases use Altona’s upscaled permeability distribution. Cases 1 through 4 model
 275 the influence of mass flow rate. Cases 5 through 10 model the influence of well separation distance along
 276 the y- and x-axis, and Cases 11 through 14 evaluate the influence of the relative well placement. E, W, N,
 277 and S denote the four Cardinal points. *Note: The direction of fluid circulation in Case 0 can be selected
 278 arbitrarily, since fluid circulation direction is inconsequential for a uniform permeability field.

Case No.	Mass flow rate, \dot{m}	Well separation distance, W_{sd}	Fluid circulation (-)
0	$20 \text{ kg} \cdot \text{s}^{-1}$	500 m	Not applicable*
1	$10 \text{ kg} \cdot \text{s}^{-1}$	500 m	W – E
2	$20 \text{ kg} \cdot \text{s}^{-1}$	500 m	W – E
3	$40 \text{ kg} \cdot \text{s}^{-1}$	500 m	W – E
4	$20 \text{ kg} \cdot \text{s}^{-1}$	300 m	W – E
5	$20 \text{ kg} \cdot \text{s}^{-1}$	400 m	W – E
6	$20 \text{ kg} \cdot \text{s}^{-1}$	500 m	W – E
7	$20 \text{ kg} \cdot \text{s}^{-1}$	300 m	N - S
8	$20 \text{ kg} \cdot \text{s}^{-1}$	400 m	N – S

9	$20 \text{ kg} \cdot \text{s}^{-1}$	500 m	N - S
10	$20 \text{ kg} \cdot \text{s}^{-1}$	500 m	W - E
11	$20 \text{ kg} \cdot \text{s}^{-1}$	500 m	N - S
12	$20 \text{ kg} \cdot \text{s}^{-1}$	500 m	NW - SE
13	$20 \text{ kg} \cdot \text{s}^{-1}$	500 m	NE - SW

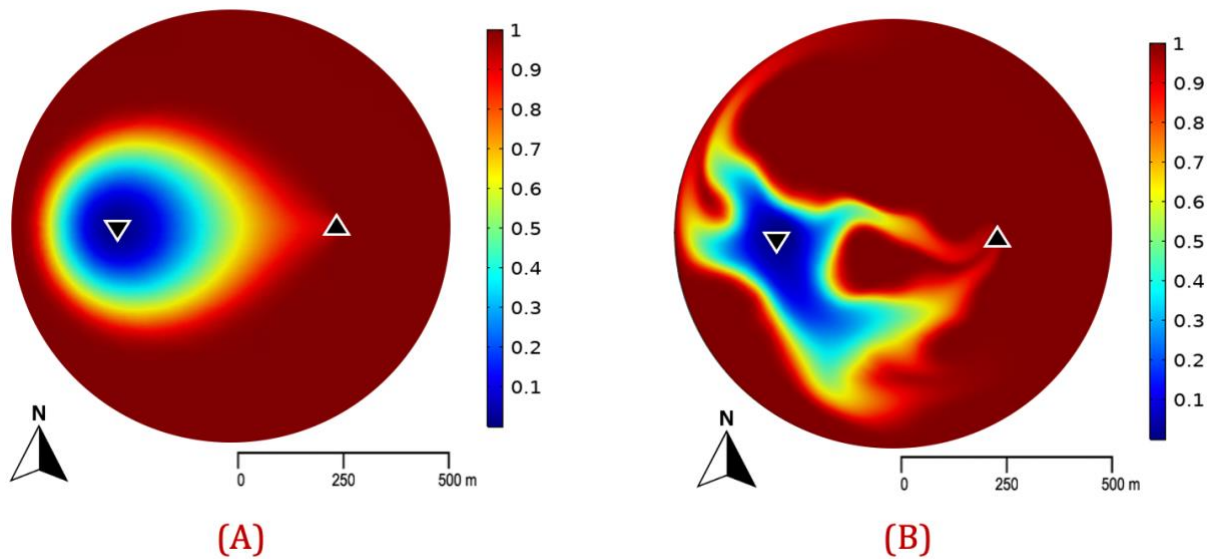
279 **Table 3.** Summary of the model parameters that were not varied in the 14-case sensitivity study described
280 in Table 2.

Parameter	Symbol	Values
Rock block height	H	100 m
Rock porosity	ϕ_r	0.1%
Specific heat capacity of the fluid	$C_{p,f}$	4184 J/(kg*K)
Specific heat capacity of the rock	$C_{p,r}$	1000 J/(kg*K)
Thermal conductivity of the fluid	k_f	0.6 W/(m*K)
Thermal conductivity of the rock	k_r	2.4 W/(m*K)
Rock density	ρ_r	2300 kg/m ³
Reinjection temperature	T_{inj}	50°C
Initial reservoir temperature	T_r	200°C
Well radius	w_r	0.15 m

281
282 Prior to conducting sensitivity analyses for the extraction parameters outlined in Table 2 above, a
283 comparison between the uniform fracture base case (Case 0) and one up-scaled spatially variable
284 fracture (Case 1) is included in this subsection. Here we discuss and quantify potential differences
285 for fluid flow and heat transport processes between homogenous and highly heterogenous
286 permeability distributions. For these simulations, we assume a constant mass flow rate of $20 \text{ kg} \cdot$
287 s^{-1} , reservoir temperature of 200°C, reinjection temperature of 50°C, and an inter-well spacing of
288 500 m from West to East. Thermal drawdown plots for these and other simulations are expressed

289 in both absolute temperature and normalized temperature to be indicative of the rate of thermal
290 depletion for any arbitrary injection and reservoir temperatures selected. In the thermal exchange
291 maps shown below, the regions that are still hot (i.e. red) correspond to areas that did not interact
292 with the cold working fluids significantly during the thermal extraction process. Whereas regions
293 that are cold (blue) are zones from where heat was extracted by the circulation of low-temperature
294 working fluids.

295



296

297 **Figure 5.** Thermal exchange maps after 1 year of geothermal extraction, for an injection well in left sector
298 (down-facing triangle) to an extraction well in the right sector (up-facing triangle). Case 0, on the left depicts
299 the dipole model that considers a constant-aperture fracture. Case 1, on the right, depicts the geothermal
300 extraction that occurs for the up-scaled permeability distribution at Altona (Figure 3). Both simulations
301 consider the following parameters: mass flow rate of $20 \text{ kg} \cdot \text{s}^{-1}$, reservoir temperature of $200 \text{ }^\circ\text{C}$, reinjection
302 temperature of $50 \text{ }^\circ\text{C}$, and an inter-well spacing of 500 m from West to East.

303

304

305

306

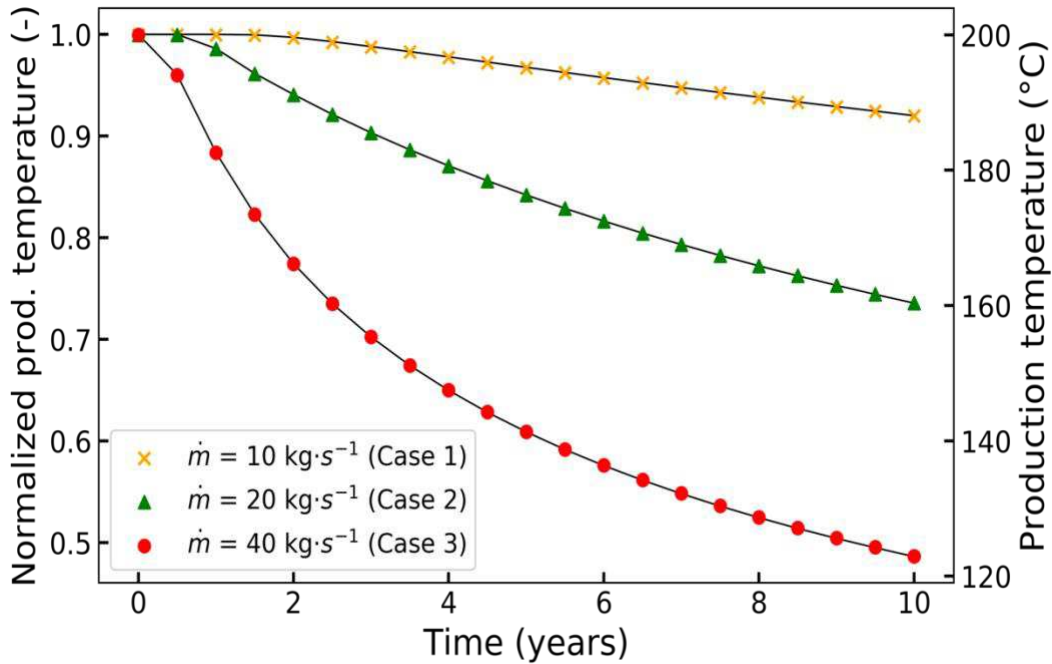
307

308

309 **Results and Discussion**

310 Figure 5 panel A exhibits ideal dipole flow along a uniformly permeable fracture, whereas the
311 thermal exchange map in panel B is characterized by highly irregular heat extraction patterns that
312 affect the thermal-hydraulic performance of the reservoir. The creation of these irregular patterns
313 will have a direct influence in the area of the fracture that is interacting with the fluids and, as a
314 result, will regulate the thermal performance of the fracture. As for the advective heat transfer
315 calculations of the base case, the fracture aperture value is irrelevant since this value in constant-
316 aperture fractures does not affect the area available for heat transfer (Hawkins et al., 2020). This
317 means that for a constant-aperture fracture system, the aperture magnitude might affect reservoir
318 volume but had no direct effect on the area available for heat transfer, thus, it does not affect
319 thermal performance estimates either.

320 The mass flow rate sensitivity analysis is conducted by specifying the spatial coordinates (x,y,z)
321 for the injection well at $(-250 \text{ m}, 0, 0)$ and production well at $(250 \text{ m}, 0, 0)$. Therefore, the inter-
322 well separation is 500 m and the fluid circulation is from West to East. The mass flow rate is varied
323 as 10, 20, and 40 kg/s and thermal performance results are simulated over the course of 10 years
324 for all cases (Figure 6). The left y-axis contains the values of normalized temperature obtained
325 using Equation 13. The right y-axis contains the absolute production temperature at the extraction
326 well in degrees Celsius, where 200°C is the original reservoir temperature ($T_{nd} = 1$) and 50 °C
327 corresponds to the reinjection temperature ($T_{nd} = 0$).

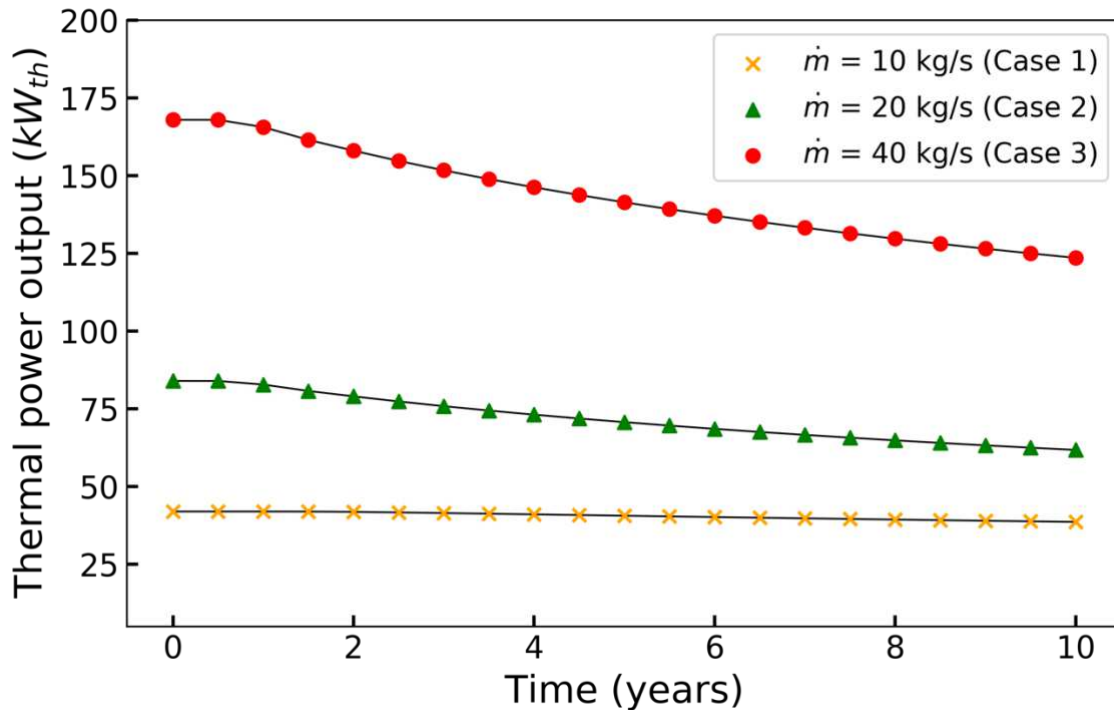


328

329 **Figure 6.** Impact of mass flow rate on the production temperatures at the extraction well. Fluid circulation
 330 occurred from West to East and the inter-well separation distance was fixed at 500 m.

331 We observe that higher production temperatures are favored by low mass flow rates due to smaller
 332 thermal loads imposed on the fracture’s surfaces intended for heat mining. Although Figure 6 may
 333 give the reader the impression that low mass flow rates lead to superior thermal performance over
 334 time, such flow rates also lead to lower power generation—both thermal and/or electric—due to a
 335 lesser volumetric throughput. In fact, although Case 3 considers the higher mass flow rate
 336 considered and consistently yielded the lowest production temperatures, this flow rate also led to
 337 the highest power production compared to all other cases (Figure 7). Therefore, an optimum mass
 338 flowrate in geothermal extraction is one that ensures the long-term generation of high-temperature
 339 production fluids while still delivering a reasonable power output. According to Clauser (2006),
 340 flow rates and production temperatures in excess of 50 kg/s and 150°C, respectively, are required
 341 to allow an economical generation of electrical energy from geothermal resources. Therefore,
 342 based on the data in Figure 6, electricity generation would not be feasible if heat extraction only
 343 occurs from one fracture displaying Altona’s up-scaled permeability. For the cases studied above,

344 a system of at least three fractures, each one mining heat at a mass flow rate of 20 kg/s would be
345 required to allow for economical electricity generation. Hence, Case 2 is selected as the base case
346 for subsequent analyses.



347

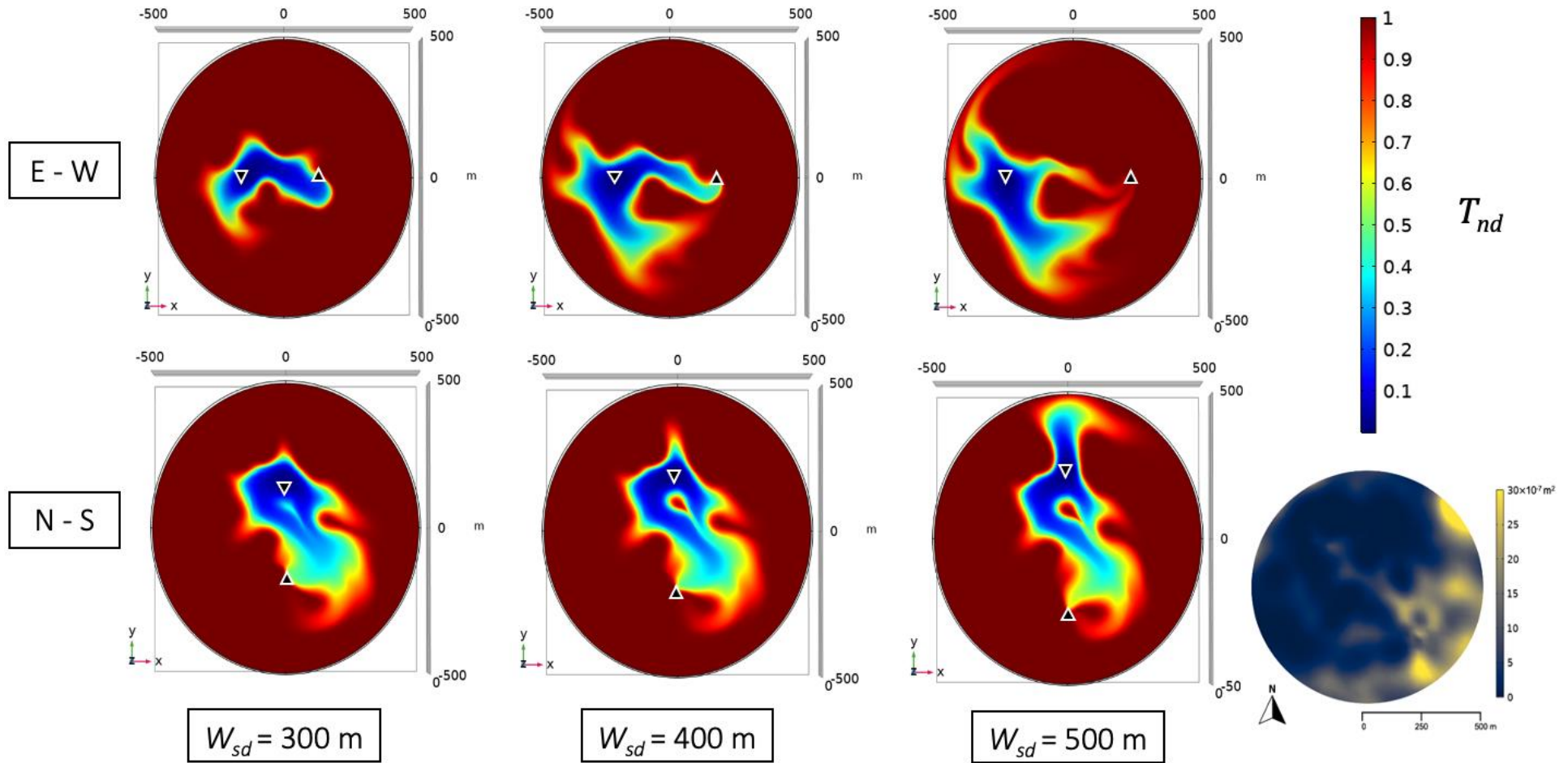
348 **Figure 7.** Impact of mass flow rate on thermal power generation. Thermal power generation was calculated
349 using $P = \dot{m}C_p\Delta T$ where P is thermal power, C_p is the specific heat capacity of the fluid and ΔT is the
350 difference between the temperature of the working fluid being produced and the reinjection temperature.

351 Since injection volumes also require a proportional energy input to pump the working fluid into
352 and out of the reservoir, a full economic analysis should consider the associated costs of parasitic
353 pumping requirements to provide an accurate estimation of its levelized cost of energy (LCOE).
354 However, LCOE calculations for this and subsequent analyses are not part of the scope of this
355 study and are recommended as future work.

356 After evaluating the influence of mass flow rate, further investigations are conducted with this
357 modeling framework to understand how sensitive the thermal performance of a heterogeneous
358 reservoir would be to variations in the inter-well separation distance. As noted by previous studies
359 (e.g. Rodemann, 1982; Ghassemi et al., 2003), when dealing with uniform permeability, well

360 separation distance has a proportional relationship on thermal performance given that increasing
361 the inter-well separation distance will proportionally increase area of the reservoir available for
362 heat transfer and dipole flow. While in general lines it is true that large separation distances
363 between injection and production wells favor higher production temperatures, Pandey et al (2018)
364 and Nicol & Robinson (1990) show that this relationship between well spacing and heat extraction
365 in heterogenous reservoirs is not linear, since the reservoir area available for heat extraction does
366 not scale proportionally with well spacing. Thus, under such conditions, thermal performance
367 improvements do not scale accordingly. In order to discover what is the relationship between well
368 spacing and heat extraction for a reservoir displaying highly heterogenous and channelized
369 hydrologic behavior, the injection and production wells are arbitrarily located at 300, 400 and 500
370 m from each other along the x-axis first, for Cases 4 through 6, respectively, and along the y-axis
371 next, for Cases 7 through 9. These sets of simulations are presented in Figures 8 and 9, respectively.

372



373

374

375

376

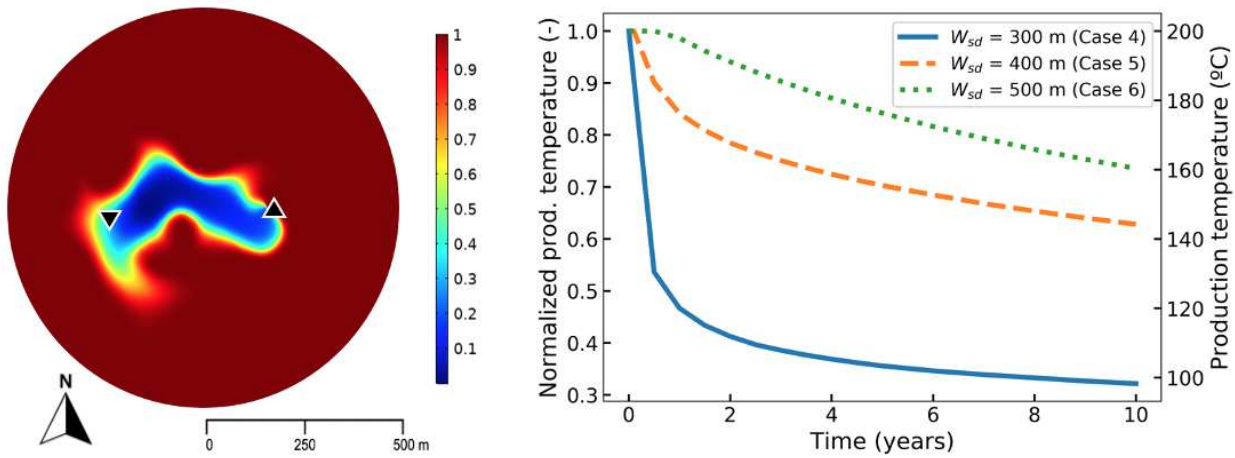
377

378

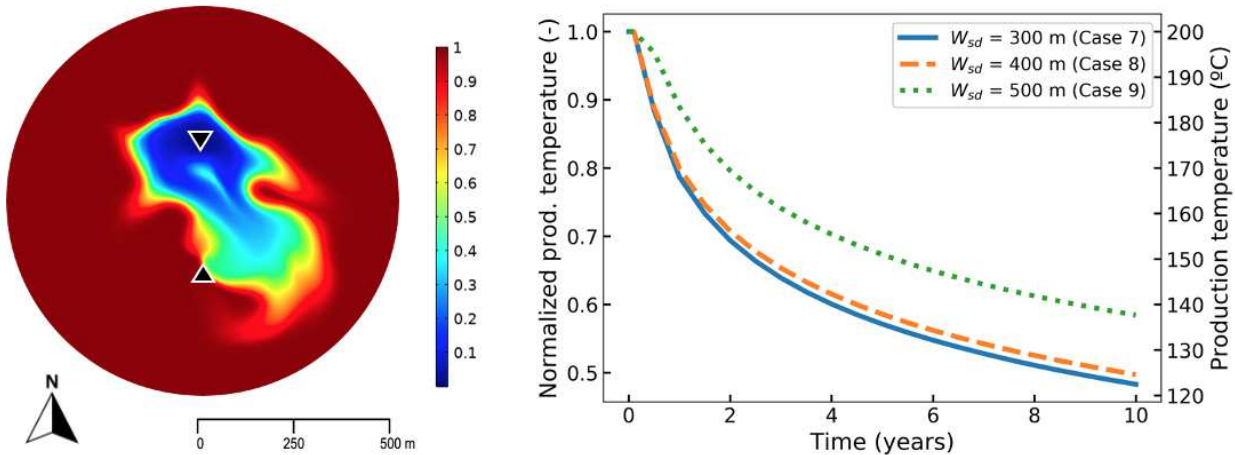
Figure 8. Temporal evolution of the thermal front advance for cases 4 through 9. Interwell separation distance varies from 300 to 500 m along the x-axis (first row) and the y-axis (second row). For the set of panels in the first row, fluid circulation occurs from an injection well in the western sector to an extraction well in the eastern sector. Fluid circulation for all panels in the second row occurs from an injection well in the northern sector to a production well in the southern sector. T_{nd} represents the reservoir's dimensionless temperature and W_{sd} represents the inter-well spacing. Columns depict thermal exchange state after 1 year of continuous operation. Image on the bottom right corner represents the up-scaled permeability distribution.

379 As shown by Figure 8, varying the well spacing from 300 to 500 m along the y-axis (i.e. Cases 7
380 through 9) has a lesser influence on the flow-wetted area available for heat transfer compared to
381 the same parameter and magnitude variation along the x-axis for Cases 4 through 6. All panels in
382 the second row of Figure 8 appear to be affected to a similar extent by fluid injection because,
383 when circulation occurs from North to South, injected fluids are readily introduced into a large
384 region where high aperture values are present, allowing fluids to short-circuit to the production
385 well, despite large well spacing variations. Conversely, for the cases shown in the first row of
386 Figure 8, we clearly observe that a progressive increase of 100 and 200 m between the injection
387 and production well, respectively, enables the fluids to be in contact with a much larger area of the
388 fracture before being extracted from the reservoir. As there are no major large-aperture channels
389 located transversally from West to East (Figure 3), the distance at which the fluids are injected
390 from the center of the fracture plays a key role in determining the fluid flow distribution through
391 other conduits that are relatively less permeable than the main channel.

Fluid circulation from West to East



Fluid circulation from North to South

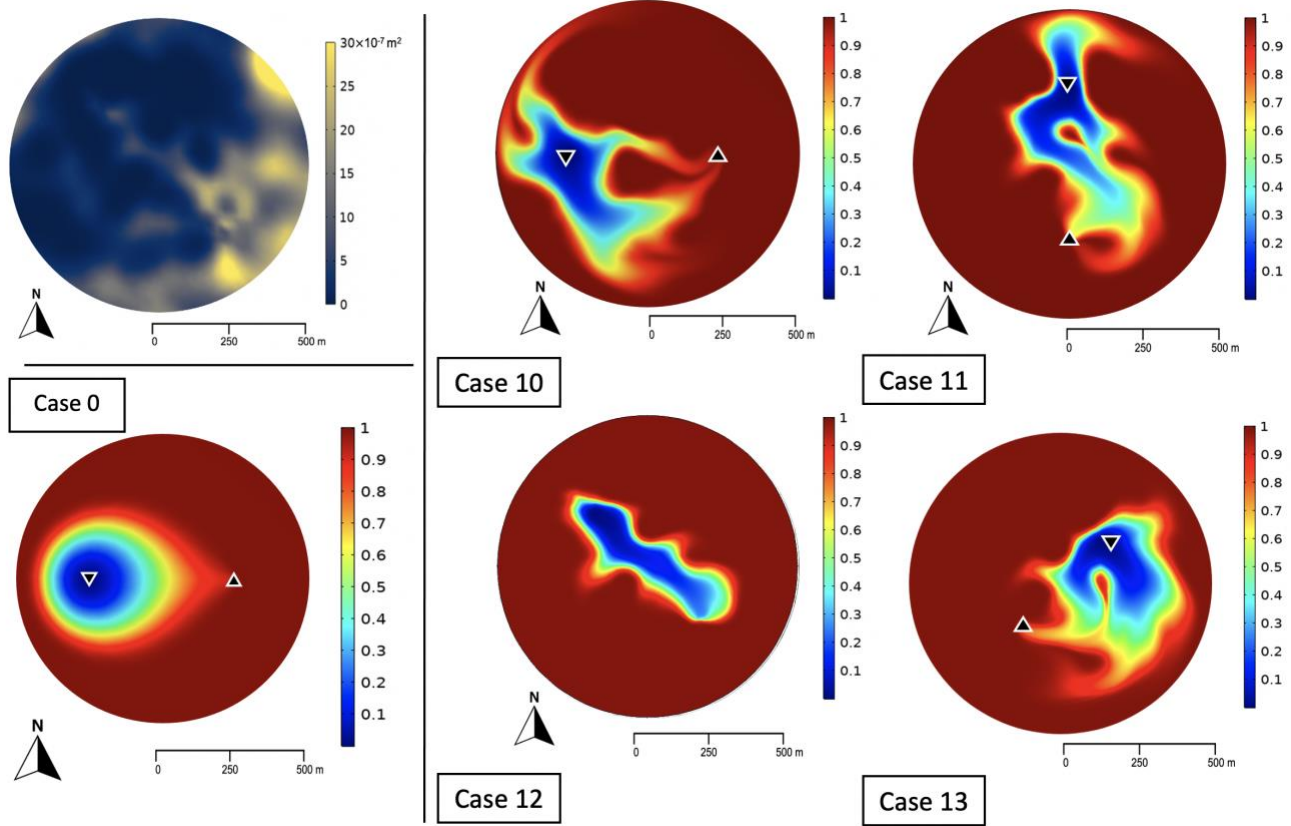


392
 393 **Figure 9.** Impact of well separation distance, along two arbitrary directions, on thermal performance. Panels
 394 in the left column show the thermal exchange map after 1 year of operation with well separation distance
 395 of 300 m in both cases. Simulated thermal drawdown plots in the second column depict the production
 396 temperature evolution for 10 years, for cases of 300 m, 400 m, and 500 m distances between the injection
 397 and production wells.

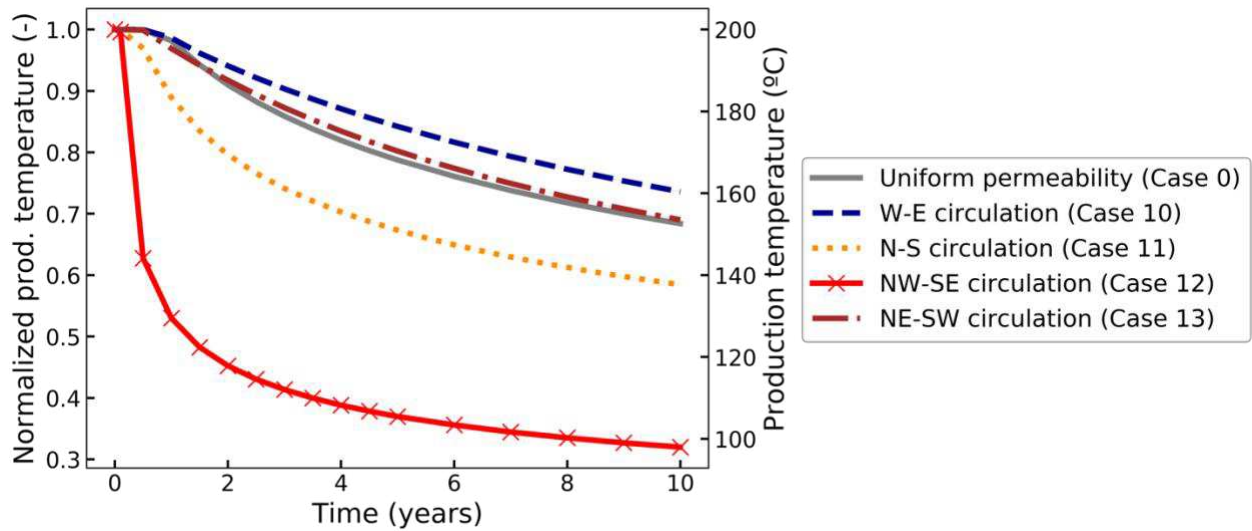
398 In presence of highly channelized fields, we observe that cumulative heat production does not
 399 scale proportionally with well separation distance (Figure 9). The difference in average power
 400 production of Case 7 ($W_{sd} = 300$ m) with Case 8 ($W_{sd} = 400$ m), and Case 8 with Case 9 ($W_{sd} =$
 401 500 m) is 1.1 kW_{th} and 6.6 kW_{th}, respectively, despite that both represent a 100 m increase in W_{sd}
 402 over the respective previous case. The same relative differences for the West to East circulation
 403 set of cases (Cases 4, 5, and 6) show a much higher variability, yielding differences in power

404 production of 26.4 kW_{th} and 10.1 kW_{th}, respectively. Furthermore, it is worth noting that, varying
405 exclusively well separation distance, leaving all other extraction parameters unchanged, the West
406 to East fluid circulation generated both the best-case scenario averaging a yearly power production
407 of 74.3 kW_{th} and worst-case scenario averaging a yearly power production of 37.8 kW_{th} for power
408 generation—for all cases considered. While the results of variations along the N-S axis were all
409 located in a narrow range of 53.2 to 60.9 kW_{th}.

410 The findings of the well separation distance variations described above are indicative of the
411 influence of the relative placement of wellbores in channelized fields. Data contained in Figure 9
412 illustrate how a relatively arbitrary parameter like well positioning can be a critical factor that is
413 either detrimental or advantageous for the thermal performance of a geothermal reservoir. To
414 reduce the uncertainty in forecasting thermal performance, the reinjection strategy in EGS will
415 ideally take into account the site-specific circulation of the fluids in the regional model. The
416 discussion above demonstrates that heat transfer in rough fractures is hindered by channeling
417 effects which is intensified by small well spacings for hydraulically isolated fractures. Considering
418 this, a series of simulations (Cases 10 through 13) are conducted for a well separation distance of
419 500 m in which only the relative placement of the well pair is varied. Based on the reference frame
420 used above and the permeability field in Figure 3, the fluid circulation is simulated in four
421 directions: West to East (W-E, Case 10), North to South (N-S, Case 11), Northwest to Southeast
422 (NW-SE; Case 12), and Northeast to Southwest (NE-SW, Case 13) with a fixed well separation
423 distance of 500 m. The rest of modeling parameters remain unchanged (Table 3).



424
425
426



427

428 **Figure 10.** Up-scaled permeability distribution on the upper left-hand side of the figure alongside simulated
 429 thermal exchange maps for Case 0, on the bottom left-hand side, and Cases 10 through 13, on the right.
 430 Below, thermal drawdown curves for all cases considering a continuous mass flow rate of $20 \text{ kg} \cdot \text{s}^{-1}$ and

431 a well separation distance of 500 m over 10 years of geothermal extraction. Thermal exchange maps depict
432 the advancement of the thermal front after 1 year of operation.

433

434 Figure 10 shows the thermal exchange maps and thermal drawdown plots of the base case with
435 uniform permeability (Case 0) and the cases where the influence of relative well placement was
436 assessed (Cases 10 through 13). Comparing the last set of simulations with an *ideal fracture* that
437 assumes constant aperture, we observe how the circulation from West to East (Case 10) and fluid
438 circulation from Northeast to Southwest (Case 13) show marginal improvements relative to the
439 thermal performance of the base case, while the production temperatures for cases in which the
440 fluid circulation occurred from North to South (Case 11) and Northwest to Southeast (Case 12)
441 significantly decreased due to extreme flow channeling. These results show that, in reservoirs
442 displaying non-uniform permeability, thermal breakthrough is highly dependent on the direction
443 of geothermal extraction and that thermal performance is negatively affected when extraction
444 occurs along in the same the direction of pre-existing main channels. However, in contrast,
445 enhanced thermal performance was observed when multiple pathways between injection and
446 production wells were used by the fluids to mine heat from the rock. When fluid circulation was
447 aligned with the most permeable feature along the NW-SE axis (Case 12), the normalized
448 production temperature dropped more than 50% within the first year of operation and by the end
449 of the tenth year this value was below 0.3 (i.e. <100°C). Although this is a dramatic decrease in
450 production temperature during a relatively short period, it is interesting to note that this extreme
451 short circuiting behavior in fractured reservoirs still performs better than a closed loop system.
452 Because closed-loop designs have limited contact area between the wellbore and the surrounding
453 rock, they are characterized by poor thermal performance, yielding production temperature drops
454 of 80% or more within the first hours of geothermal extraction (Beckers et al., 2022).

455 In contrast to the scenario in which well alignment is parallel to the permeable channel, a well
456 alignment in the perpendicular direction (fluid circulation from Northeast to Southwest), still has
457 flow restricted to a small area of the fracture (Figure 10), but the cumulative power production for
458 this scenario (Case 13; 5,519 MW-hr) was almost 2.2 times larger than that of Case 12 (2,533
459 MW-hr).

460 All cases in this section assume no-flow boundaries around the fracture, hence, the consequences
461 of lost circulation into the formation are not considered. Our assumptions consider the fracture is
462 hydraulically isolated from the formation and that 100% recovery factor of the injected fluids is
463 ensured, hence, hydraulic performance is not studied in detail in this work. However, thermal
464 performance and hydraulic performance must be balanced to ensure the viability of any geothermal
465 project. A reservoir too large in size would increase the area available for heat transfer but would
466 also make it much more challenging to retrieve the injected fluid. According to Armstead and
467 Tester (1987), water loss into the formation is inevitable in EGS, but having a loss rate greater than
468 5% is not acceptable. Both Clauser (2006) and MIT (2006) estimate that economic flow rates of
469 geothermal systems intended for electricity generation should exceed 50 kg/s. A large pressure
470 drop between the injection and production wells may impede such flow rates at the production
471 well. Future work on thermal-hydraulic numerical modeling of discretely fractured reservoirs
472 should account for fluid circulation loss by imposing open-flow boundaries surrounding the model
473 domain.

474 Additionally, for simplicity, all of our models assume that freshwater is being injected to the
475 reservoir and that it is the same fluid composition that is being extracted at the production well.
476 For instance, the unintended production of subsurface brines would also influence fluid flow and
477 heat transfer in thermal aquifers. Since the density of brine is higher, by using freshwater, the total
478 amount of thermal energy in the formation is lower, yet its heat capacity is smaller. This means
479 that freshwater would have a higher heat extraction rate than brine (Smith, 2019; Ramalingam and

480 Arumugam, 2012). Similarly, several studies suggest that the unique thermodynamic properties of
481 supercritical CO₂ make this fluid attractive for subsurface extraction of thermal energy (Brown,
482 2000; Pruess, 2006; Randolph & Saar, 2011). However, having a much lower viscosity—
483 compared to freshwater—CO₂ can be more prone to flow-channeling in non-uniform permeability
484 fields. Thus, a sensitivity analysis on the chemical composition of the working fluid using
485 freshwater, multiple brines, supercritical CO₂, among others, is also recommended for future work.

486 **Conclusions**

487 In most enhanced geothermal systems (EGS) and other fracture-dominated reservoirs, faults and
488 fractures are the main conduits for fluid flow and heat transfer. Since rock fractures are rough in
489 nature, they inherently create non-uniform permeability fields along reservoir surfaces. The
490 resulting permeability distributions introduce dramatic variability into the long-term thermal
491 performance of a given reservoir. The existence of non-uniform permeability introduces thermal
492 performance uncertainty that is a major barrier to attracting financial investment in geothermal
493 energy, particularly enhanced geothermal systems. This is because enhanced geothermal systems
494 are most commonly conduction-limited rather than convection-limited reservoirs. In a conduction-
495 limited setting, if non-ideal heterogeneities result in insufficient heat transfer surface area, then
496 thermal interference may occur between injection and production wells prior to the project
497 reaching financial maturity, which may be disastrous for a commercial operation which requires
498 high capital investment just to drill a single exploration well (Brown, 1987; Murphy et al., 1981;
499 Robinson and Tester, 1988; Tsang & Neretnieks, 1997). Nonetheless, closed-loop geothermal
500 systems appear to be even more affected by the limited heat transfer surface area than fractured
501 reservoirs, yielding even more discrete thermal performance estimates (Beckers et al., 2022).

502 In the context of non-uniform permeability reservoirs, going from theoretical studies to field-
503 constrained models is important because evidence of flow channeling observed at meso-scale
504 reservoirs (Altona in particular) is more extreme than what has been observed in random aperture
505 fields before (Neuvile et al., 2010; Fox et al., 2015) and previous core and outcrop studies

506 (Okoroafor & Horne, 2021; Candela et al., 2009; Glover et al., 1998). This work highlights the
507 need to construct numerical models that can ground truth thermal performance for EGS somewhere
508 between the idealized scenarios that consider uniform permeability and more realistic, highly-
509 heterogeneous fields like Altona where thermal performance is dramatically poor due to fluid flow
510 short circuiting.

511 Although up-scaling petrophysical properties is challenging for rocks that exhibit multimodal
512 porosity (Cobett et al., 2016; Glover et al., 1998), our analyses show that up-scaled synthetic
513 fractures from meso-scale data can provide insightful information on the hydraulic and thermal
514 performance of field fractures. For the cases we studied, variations in the mass flow rate affect the
515 thermal performance of highly channelized fields significantly. High mass flow rates, which would
516 be preferred for ideal fractures with uniform aperture, might result in disastrous rates of thermal
517 drawdown in channelized fractures. In such cases, multiple parallel fractures that distribute the
518 working fluids evenly are preferred over increasing the mass flow rate through a single fracture to
519 increase volumetric throughput. Additionally, well separation distance and well relative
520 positioning proved to be critical factors in the success or failure of geothermal reservoirs
521 displaying non-uniform permeability. As opposed to homogeneous reservoirs, their influence in
522 highly channelized reservoirs is not trivial and it is often disregarded in numerical studies. Rather,
523 understanding how the hydrothermal behavior is affected by heterogeneous subsurface
524 permeability can help to determine what is the optimal well separation distance and the optimal
525 places to drill geothermal well-pairs and/or if additional connectivity is needed in between the
526 wells. To avoid fluid flow channeling and maximize power production for a given reservoir,
527 thoughtful positioning of the wellbores can be done in accordance with a prior identification of the
528 dimensions and orientation of the most permeable structures. In such cases, even in the presence
529 of highly-channelized fields, premature thermal breakthrough can be mitigated and ideal thermal
530 performance is achieved.

531

532 **Availability of data and materials**

533 The datasets used and/or generated during the current study are available from the corresponding
534 author on reasonable request.

535 **Competing interests**

536 The authors declare that they have no known competing financial interests or personal
537 relationships that could have influenced the work reported in this article.

538 **Funding**

539 This work was partially funded by the U.S. Department of Energy-funded project for deep direct-
540 use of geothermal energy at Cornell University (Award Number DE-EE0008103) and by the U.S.
541 Department of Energy-funded project for Innovative Methods to Control Hydraulic Properties of
542 Enhanced Geothermal Systems (Award Number DE-FOA-0002498).

543 **Authors' contributions**

544 **NRJ:** Investigation, Formal analysis, Software, Manuscript writing – review and editing.
545 **AJH:** Supervision, Funding, Writing – review & editing. **PMF:** Supervision, Funding, Writing –
546 review & editing. All authors read and approved the final manuscript.

547 **Acknowledgements**

548 The authors would like to thank Jefferson Tester and Terry Jordan for providing valuable insights
549 on geothermal systems engineering and reservoir characterization, and Ivan Purwamaska for
550 providing help with COMSOL modeling.

551

552 **References**

- 553 Armstead, H. C., & Tester, J. W. Heat Mining. 1987.
554 Armstead, H. C., & Tester, J. W. The future of geothermal energy. In J. Inst. Fuel. 1978; Vol 51.
555 Beckers, K. F., Rangel-Jurado, N., Chandrasekar, H., Hawkins, A. J., Fulton, P. M. & Tester, J. W.
556 Techno-Economic Performance of Closed-Loop Geothermal Systems for Heat Production and
557 Electricity Generation. Geothermics.2022; <https://doi.org/10.1016/j.geothermics.2021.102318>
558 Brown, D. A hot dry rock geothermal energy concept utilizing supercritical CO₂ instead of water, in
559 Proceedings of the Twenty-Fifth Workshop on Geothermal Reservoir Engineering, 2000;233–238.
560 Brown, S. R. Fluid flow through rock joints: the effect of surface roughness. Journal of Geophysical
561 Research, 1987; 1337–1347. <https://doi.org/10.1029/JB092iB02p01337>
562 Bruderer-Weng, C., Cowie, P., Bernabé, Y., & Main, I. Relating flow channelling to tracer dispersion in
563 heterogeneous networks. Advances in Water Resources. 2004; 27(8), 843–855.
564 <https://doi.org/10.1016/j.advwatres.2004.05.001>

565 Bundschuh, J., & César Suárez A., M. Introduction to the Numerical Modeling of Groundwater and
566 Geothermal Systems. In Introduction to the Numerical Modeling of Groundwater and Geothermal
567 Systems. 2010; <https://doi.org/10.1201/b10499>

568 Candela, T., Renard, F., & Bouchon, M. Characterization of Fault Roughness at Various Scales:
569 Implications of Three-Dimensional High Resolution Topography Measurements. Pure Applied
570 Geophysics. 2009; <https://doi.org/10.1007/s00024-009-0521-2>

571 Chandrasekharam, D., & Bundschuh, J. Low-enthalpy Geothermal Resources for Power Generation
572 Energy Sources, Part A: Recovery, Utilization, and Environmental Effects, 2008; 31(1), 98.
573 <https://doi.org/10.1080/15567030802557058>

574 Clauser, C. Geothermal energy. Advanced Material and Technologies. 2006

575 Comsol. Subsurface Flow Module. In COMSOL Multiphysics Reference Manual. 2019.
576 https://doc.comsol.com/5.5/doc/com.comsol.help.comsol/COMSOL_ReferenceManual.pdf

577 Corbett, P. W. M., Jensen, J. L., & Sorbie, K. S. A review of up-scaling and cross-scaling issues in core
578 and log data interpretation and prediction. Geological Society Special Publication. 1998; 136, 9–16.
579 <https://doi.org/10.1144/GSL.SP.1998.136.01.02>

580 Farmer, C. L. Upscaling: A review. International Journal for Numerical Methods in Fluids. 2002;40(1–2),
581 63–78. <https://doi.org/10.1002/flid.267>

582 Fox, D. B., Koch, D. L., & Tester, J. W. The effect of spatial aperture variations on the thermal
583 performance of discretely fractured geothermal reservoirs. 2015; [https://doi.org/10.1186/s40517-](https://doi.org/10.1186/s40517-015-0039-z)
584 [015-0039-z](https://doi.org/10.1186/s40517-015-0039-z)

585 Ghassemi, A., Tarasovs, S., & Cheng, A. H. D. An integral equation solution for three-dimensional heat
586 extraction from planar fracture in hot dry rock. International Journal for Numerical and Analytical
587 Methods in Geomechanics. 2003; 27(12), 989–1004. <https://doi.org/10.1002/nag.308>

588 Ghassemi, A., Tarasovs, S., & Cheng, A. H. D. Integral equation solution of heat extraction-induced
589 thermal stress in enhanced geothermal reservoirs. International Journal for Numerical and Analytical
590 Methods in Geomechanics. 2005; 29(8), 829–844. <https://doi.org/10.1002/nag.440>

591 Glover, P. W. J., Matsuki, K., Hikima, R., & Hayashi, K. Fluid flow in synthetic rough fractures and
592 application to the Hachimantai geothermal hot dry rock test site. Journal of Geophysical Research:
593 Solid Earth. 1998;103(5), 9621–9635. <https://doi.org/10.1029/97jb01613>

594 Gringarten, A. C., & Sauty, J. P. A Theoretical Study of Heat Extraction From Aquifers With Uniform
595 Regional Flow. Journal of Geophysical Research. 1975; 130(35), 107–109.

596 Hawkins, A. J. Reactive Tracers for Characterizing Fractured Geothermal Reservoirs. Cornell University.
597 PhD Dissertation. 2017

598 Hawkins, A. J., Becker, M. W., & Tester, J. W. Inert and Adsorptive Tracer Tests for Field Measurement
599 of Flow-Wetted Surface Area. Water Resources Research. 2018; 54(8), 5341–5358.
600 <https://doi.org/10.1029/2017WR021910>

601 Hawkins, A. J., Becker, M. W., & Tsoflias, G. P. Evaluation of inert tracers in a bedrock fracture using
602 ground penetrating radar and thermal sensors. Geothermics. 2017; 67, 86–94.
603 <https://doi.org/10.1016/j.geothermics.2017.01.006>

604 Hawkins, A. J., Fox, D. B., Becker, M. W., & Tester, J. W. Measurement and simulation of heat exchange
605 in fractured bedrock using inert and thermally degrading tracers. Water Resources Research. 2017;
606 5(3), 2–2. <https://doi.org/10.1111/j.1752-1688.1969.tb04897.x>

607 Hawkins, A. J., Fox, D. B., Koch, D. L., Becker, M. W., & Tester, J. W. Predictive Inverse Model for
608 Advective Heat Transfer in a Short-Circuited Fracture: Dimensional Analysis, Machine Learning,
609 and Field Demonstration. Water Resources Research. 2020; 56(11), 1–20.
610 <https://doi.org/10.1029/2020WR027065>

611 Huang, W., Cao, W., & Jiang, F. Heat extraction performance of EGS with heterogeneous reservoir: A
612 numerical evaluation. International Journal of Heat and Mass Transfer. 2017; 108, 645–657.
613 <https://doi.org/10.1016/j.ijheatmasstransfer.2016.12.037>

614 Hui, M. H. R., Karimi-Fard, M., Mallison, B., & Durlofsky, L. J. A general modeling framework for
615 simulating complex recovery processes in fractured reservoirs at different resolutions. *SPE Journal*.
616 2018; 23(2), 598–613. <https://doi.org/10.2118/182621-pa>

617 Kolditz, O. & Clauser, C. Numerical simulation of flow and heat transfer in fractured crystalline rocks:
618 application to the hot dry rock site in Rosemanowes (U.K.) *Geothermics*. 1998; 1-23.

619 Lu, S. M. A global review of enhanced geothermal system (EGS). *Renewable and Sustainable Energy*
620 *Reviews*. 2018.

621 Massachusetts Institute of Technology (MIT). *The Future of Geothermal Energy The Future of*
622 *Geothermal Energy*. In *Technology: Vol. Im (Issue November)*. 2006.

623 Murphy, H. D., Tester, J. W., Grigsby, C. O., & Potter, R. M. Energy extraction from fractured
624 geothermal reservoirs in low- permeability crystalline rock. *Journal of Geophysical Research*. 1981;
625 86(B8), 7145–7158. <https://doi.org/10.1029/JB086iB08p07145>

626 National Research Council. *Rock Fractures and Fluid Flow: Contemporary Understanding and*
627 *Applications*. The National Academies Press. 1996; <https://doi.org/10.17226/2309>

628 Neuville, A., Toussaint, R., & Schmittbuhl, J. Fracture roughness and thermal exchange: A case study at
629 Soultz-sous-Forêts. *Comptes Rendus - Geoscience*, 342(7–8), 616–625. 2010;
630 <https://doi.org/10.1016/j.crte.2009.03.006>

631 Nicol, D. A. C., & Robinson, B. A. Modelling the heat extraction from the rosemanowes HDR reservoir.
632 *Geothermics*. 1990; 19(3), 247–257. [https://doi.org/10.1016/0375-6505\(90\)90045-D](https://doi.org/10.1016/0375-6505(90)90045-D)

633 Ogino, F., Yamamura, M., & Fukuda, T. Heat transfer from hot dry rock to water flowing through a
634 circular fracture. *Geothermics*. 1999; 28(1), 21–44. [https://doi.org/10.1016/S0375-6505\(98\)00043-1](https://doi.org/10.1016/S0375-6505(98)00043-1)

635 Okoroafor, E. R., Williams, M. J., Gossuin, J., Jimoh-kenshiro, O., Horne, R. N., Rita, E., Williams, M.
636 J., Gossuin, J., Jimoh-kenshiro, O., & Horne, R. N. Comparison of EGS Thermal Performance with
637 CO₂ and Water as Working Fluids. *Stanford Geothermal Conference Proceedings*, 2021; 46, 1–10.

638 Olcott, P. *Ground Water Atlas of the United States*. 1995.

639 Pandey, S. N., Vishal, V., & Chaudhuri, A. Geothermal reservoir modeling in a coupled thermo-hydro-
640 mechanical-chemical approach: A review. *Earth-Science Reviews*. 2018; 1157–1169.
641 <https://doi.org/10.1016/j.earscirev.2018.09.004>

642 Pandey, S. N., & Vishal, V. Sensitivity analysis of coupled processes and parameters on the performance
643 of enhanced geothermal systems. *Scientific Reports*, 2017; 7(1). [https://doi.org/10.1038/S41598-](https://doi.org/10.1038/S41598-017-14273-4)
644 [017-14273-4](https://doi.org/10.1038/S41598-017-14273-4)

645 Pruess, K. Enhanced geothermal systems (EGS) using CO₂ as working fluid—A novel approach for
646 generating renewable energy with simultaneous sequestration of carbon, *Geothermics*. 2006; 35,
647 351–367, <https://doi.org/10.1016/j.geothermics.2006.08.002>

648 Ramalingam, A., & Arumugam, S. Experimental Study on Specific Heat of Hot Brine for Salt Gradient
649 Solar Pond Application. 2012.

650 Randolph J.B. & Saar M.O. Combining geothermal energy capture with geologic carbon dioxide
651 sequestration. *Geophys Res Letters*. 2011; 38:L10401.

652 Rayburn, J. A., Knuepfer, P. L. K., & Franzi, D. A. A series of large, Late Wisconsinan meltwater floods
653 through the Champlain and Hudson Valleys, New York State, USA. *Quaternary Science Reviews*.
654 2005; 24, 2410–2419. <https://doi.org/10.1016/j.quascirev.2005.02.010>

655 Robinson, B. A., & Tester, J. W. DISPERSED FLUID FLOW IN FRACTURED RESERVOIRS: AN
656 ANALYSIS OF TRACER-DETERMINED RESIDENCE TIME DISTRIBUTIONS. *Journal of*
657 *Geophysical Research*. 1984; 89(B12), 10374–10384. <https://doi.org/10.1029/JB089iB12p10374>

658 Rodemann H. Analytical model calculations on heat exchange in a fracture. In *Urach Geothermal Project*,
659 Haenel R (ed.). Stuttgart, 1982; 351–353.

660 Smith, J. Exploratory spatial data analysis and uncertainty propagation for geothermal resource
661 assessment and reservoir models. Cornell University. PhD Dissertation. 2019.

662 Tsang, C. & Neretnieks, I. Flow Channeling in Heterogeneous Fractured Rocks. *Reviews of Geophysics*.
663 1997; <https://escholarship.org/uc/item/8zw551hg>

664 Watanabe, N., Wang, W., McDermott, C. I., Taniguchi, T., & Kolditz, O. Uncertainty analysis of thermo-
665 hydro-mechanical coupled processes in heterogeneous porous media. *Computational Mechanics*.
666 2010; 45(4), 263–280. <https://doi.org/10.1007/s00466-009-0445-9>
667 Witherspoon, P. A., Wang, J. S. Y., Iwai, K., & Gale, J. E. Validity of Cubic Law for Fluid Flow in a
668 Deformable Rock Fracture. *WATER RESOURCES RESEARCH*. 1980; 16(6), 1016–1024.
669 Yavari, A., Sarkani, S., & Moyer, E. T. The mechanics of self-similar and self-affine fractal cracks.
670 *International Journal of Fracture*. 2002;114(1), 1–27. <https://doi.org/10.1023/A:1014878112730>
671 Zimmerman, R. W., Bodvarsson, G. S., & Bodvarsson, G. S. Hydraulic Conductivity of Rock Fractures.
672 1994.c
673
674